ADVANCED FUNCTIONAL MATERIALS
www.afm-journal.de

An Ion-Exchange Phase Transformation to $ZnGa_2O_4$ Nanocube Towards Efficient Solar Fuel Synthesis

Shicheng Yan, Jiajia Wang, Honglin Gao, Nanyan Wang, He Yu, Zhaosheng Li, Yong Zhou,* and Zhigang Zou**

To realize practical applications of the photocatalysis technique, it is necessary to synthesize semiconductor photocatalysts with specific facets that induce high reactive activities and high reactive selectivity. However, a challenge lies in the synthesis of metal oxides containing more than one type of metal with specific facets. Usually, surfactants are used to control the crystal morphology, which induces surface contamination for the final products. Here, using the GaOOH nanoplate as precursor, $ZnGa_2O_4$ nanocubes with exposed {100} facets are synthesized by an hydrothermal ion-exchange route without requiring the introduction of morphology controlling agents. These $ZnGa_2O_4$ nanocubes exhibit improved performance in the photoreduction of CO_2 into CH_4 or water splitting into hydrogen. Theoretical calculations indicates that the light-hole effective mass on the {100} facets of $ZnGa_2O_4$ corresponds to the high hole mobility, which contributes to the efficient water oxidation to offer the protons for promoting CO_2 photoreduction into hydrocarbon fuels.

1. Introduction

Photocatalysis is a promising technique to solve the problems of energy shortage and global warming, because this technique uses solar energy to split water into hydrogen fuel or, alternatively, to reduce carbon dioxide into hydrocarbon fuels. However, to realize the application of this technique, a high-activity photocatalyst is required. Recently, much research interest has been focused on semiconductor crystals with specific facets that induce high reactive activities and high reactive selectivity.[1] Attempts to deliberately fabricate such materials are challenged by the thermodynamic growth mechanisms of the crystals. Usually selective absorption of surfactants or ions on high-energy facets has been employed to suppress the growth rate along their axes. Typically, using hydrofluoric acid as a morphology controlling agent, TiO_2 nanocrystals with a high percentage of {001} facets are synthesized.[2] A major defect in the using morphology controlling agent to synthesize nanocrystals is the unavoidable surface contamination due to the residue of surfactants or ions. These residues may affect the photocatalytic reaction process, especially for the photoreduction of CO_2.[3] Therefore, a synthetic route without the use of morphology controlling agent is expected to yield a high-quality photocatalyst with a clean surface and high activity.

$ZnGa_2O_4$ is a good photocatalyst used in wastewater treatment and hydrogen production from water splitting.[4] In the past few years, $ZnGa_2O_4$ nanowires and nanocubes have been synthesized using various methods, such as solid-state reactions and chemical vapor deposition.[5] However, high reaction temperatures (1000 °C) are usually needed to synthesize $ZnGa_2O_4$. Recently, we have developed a room temperature reactive template route to fabricate mesoporous $ZnGa_2O_4$, and demonstrated that the $ZnGa_2O_4$ has a promising application in the photoreduction of CO_2 into hydrocarbon fuel.[6] In this article, we demonstrate a novel method for preparing $ZnGa_2O_4$ nanocubes with {100} facets by an ion-exchange process using the GaOOH single crystal nanoplate as a precursor without requiring the introduction of morphology controlling agents. The $ZnGa_2O_4$ nanocubes with exposed {100} facets exhibited an improved performance in the photoreduction of CO_2 into CH_4 and water splitting into hydrogen. The theoretical calculations indicated that the {100} facets have lighter hole effective mass compared with the bulk-$ZnGa_2O_4$. Light-hole effective mass corresponds to the high hole mobility on the {100} facets which contributes to the efficient water oxidation to provide protons for promoting CO_2 photoreduction.

Prof. S. C. Yan, Dr. J. J. Wang, Dr. H. L. Gao, Prof. Z. S. Li
Department of Materials Science and Engineering
College of Engineering and Applied Sciences
22 Hankou Road, Nanjing, Jiangsu 210093, China
E-mail: yscfei@nju.edu.cn
N. Y. Wang, H. Yu, Prof. Y. Zhou, Prof. Z. G. Zou
Eco-Materials and Renewable Energy Research Center (ERERC)
National Laboratory of Solid State Microstructures
Nanjing University
22 Hankou Road, Nanjing, Jiangsu 210093, China
E-mail: zhouyong1999@nju.edu.cn; zgzou@nju.edu.cn

DOI: 10.1002/adfm.201202042

2. Results and Discussion

2.1. Room Temperature ion-exchange Route to Synthesize GaOOH Nanoplates

The GaOOH was synthesized by the ion-exchange reaction of $KGaO_2 + CH_3COOH \rightarrow GaOOH + CH_3COOK$ at room

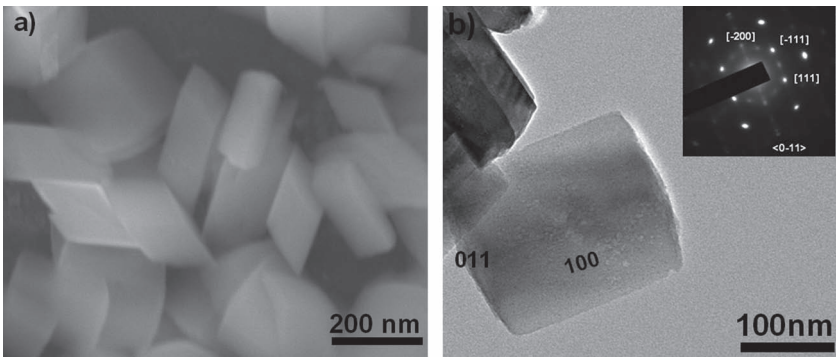

Figure 1. Characterization of GaOOH nanoplates. a) SEM image and b) TEM image (inset shows the selected area electron diffraction).

temperature. The $KGaO_2$ powder can be dispersed in water to form a suspension. When the suspension is illuminated with a 532 nm laser, the Tyndall effect is observed, that is, the suspension behaves as a colloid (see Figure S1 in the Supporting Information). Transmission electron microscopy (TEM) revealed that the $KGaO_2$ colloidal particles were uniformly dispersed in water, having an average particle size of about 20 nm (see Figure S2a in the Supporting Information). High-resolution TEM analysis indicated that the colloidal particle were devoid of a crystal lattice (see Figure S2b in the Supporting Information). This implies that the $KGaO_2$ colloidal particles are amorphous. When H^+ from CH_3COOH was introduced into the $KGaO_2$ colloidal suspension, a white precipitation appears due to the ion-exchange reaction between K^+ and H^+.

The X-ray diffraction (XRD) pattern (see Figure S3 in the Supporting Information) shows that this white precipitation can be indexed as an orthorhombic GaOOH with cell constants of a = 4.573, b = 9.804, and c = 2.972 Å, which is in good agreement with JCPDS 06–0180. The scanning electron microscopy (SEM) and TEM observations (**Figure 1**) reveal the presence of GaOOH nanoplates (about 300 nm in length and 150 nm in width) morphology with the rhombic cross section. Selected area electron diffraction (SAED) observation indicates that the GaOOH nanoplate is a single crystal. The exposed facets are {011} and {100}, as shown in Figure 1b. The time-dependent observation of the formation of GaOOH nanoplates indicated that with increasing the reaction time, the nanosheet with the dominant {100} facet first formed and then assembled along the {011} facet to form the GaOOH nanoplate (see Figure S4 in the Supporting Information).

2.2. Hydrothermal ion-exchange Route to $ZnGa_2O_4$ Nanocube Using the GaOOH Nanoplate as Precursor

The $ZnGa_2O_4$ nanocube was synthesized by hydrothermal ion-exchange reaction using the as-prepared single-crystal GaOOH nanoplate as precursor. The XRD analysis (**Figure 2**a) confirmed that the $ZnGa_2O_4$ belongs to cubic system with the cell parameter of a = 8.335 Å, corresponding to JCPDS 38–1240. SEM observation (Figure 2b) presents that the as-prepared $ZnGa_2O_4$ has the cube morphology with the particle size of about 400 nm. According to the crystallographic symmetry, the $ZnGa_2O_4$ cube can be indexed to the {100} facets exposed single crystal. To investigate the formation mechanism of $ZnGa_2O_4$ nanocube, the hydrothermal treatment of GaOOH nanoplate aqueous suspension was carried out at 200 °C for 5 h. The XRD and SEM analysis (see Figure S5 in Supporting Information) indicated that the GaOOH is stable under hydrothermal treatment, as demonstrated in the previous report.[7] This evidence supported that the ion-exchange reaction of GaOOH + $Zn(CH_3COO)_2 \rightarrow ZnGa_2O_4 + CH_3COOH$ was achieved by the Zn^{2+} diffusing into the GaOOH nanoplate.

The phase formation of $ZnGa_2O_4$ depends strongly on the weakly acidic salt $Zn(CH_3COO)_2$. The substitution of zinc salt of a strong acid such as $Zn(NO_3)_2$ or $ZnCl_2$ for $Zn(CH_3COO)_2$ will cause the ion-exchange reaction not to occur, probably due to the suppression effect of strong acid for the $ZnGa_2O_4$ formation. Indeed, an additional hydrothermal experiment demonstrated that the $ZnGa_2O_4$ is not stable in the HCl or HNO_3 aqueous solution. In addition, one-step hydrothermal synthesis by directly mixing the $KGaO_2$, CH_3COOH, and $Zn(CH_3COO)_2$ was carried out, and the final product was mesoporous $ZnGa_2O_4$, the mesostructure of which resulted from the aggregation of $ZnGa_2O_4$ nanocrystals (see Figure S6 in the Supporting Information). This means that the formation of $ZnGa_2O_4$ nanocubes is tightly associated with the precursor GaOOH nanoplate. To confirm this fact, the semifinished product of GaOOH single crystal nanoplate obtained by the ion-exchange reaction of $KGaO_2$ and CH_3COOH, which has a nanostep microstructure exhibiting an intermediate process of crystal growth, was used as the precursor to prepare the $ZnGa_2O_4$. The final product was $ZnGa_2O_4$ nanoparticles with no specific morphology (see Figure S7 in the Supporting Information), further demonstrating that the formation of $ZnGa_2O_4$ nanocubes is dependent on the GaOOH nanoplate.

The ion-exchange induced single-crystal to single-crystal phase transformation has been demonstrated in synthesizing flexible metal-organic frameworks (MOFs).[8] This can be attributed to the fact that the MOFs have a porous structure which can compensate

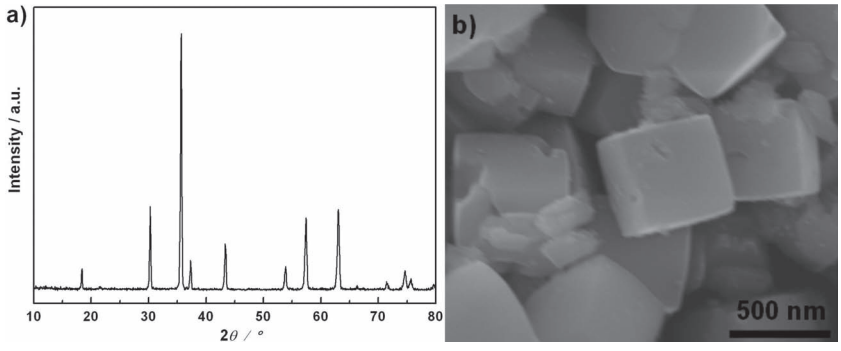

Figure 2. Characterization of $ZnGa_2O_4$ nanocube. (a) XRD pattern and (b) SEM image.

for the volume change during the single-crystal phase transformation by tuning the pore size. In our case of the ion-exchange induced single-crystal phase transformation between orthorhombic GaOOH and cubic $ZnGa_2O_4$, the time-dependent observations of the formation of $ZnGa_2O_4$ nanocube (see Figure S8 in the Supporting Information) indicated that the ion-exchange reaction occurs based on the GaOOH nanoplate, that is, the $ZnGa_2O_4$ nanocubes formed and grew on the GaOOH nanoplate, similar to the reported single-crystal phase transformation in the MOFs. The theoretical volume expansion for the phase transformation from GaOOH to $ZnGa_2O_4$ is about 8%, which results from the difference in crystal structure. The 8% of volume expansion would induce stress during the phase transformation from GaOOH to $ZnGa_2O_4$. Therefore, a slow phase transformation rate is needed for stress relaxation via an atomic reconfiguration process on the interface between GaOOH and $ZnGa_2O_4$.

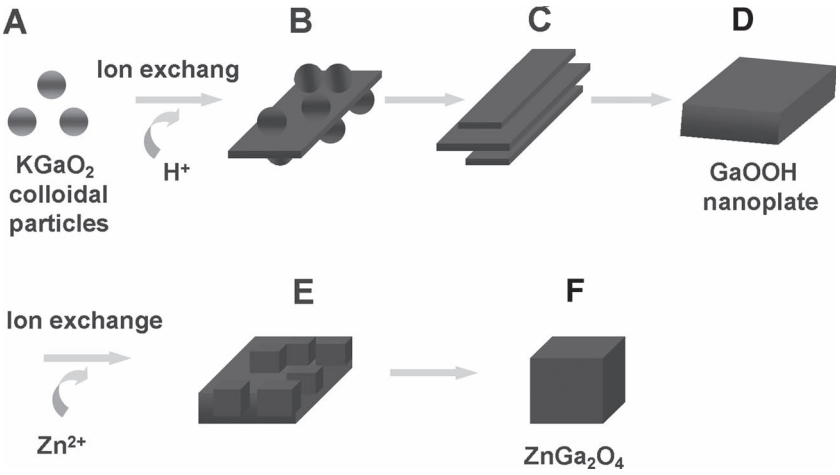

Figure 3. Illustration of the formation of $ZnGa_2O_4$ by an ion-exchange reaction based on GaOOH nanoplates. A) $KGaO_2$ colloidal particles obtained by dispersing the $KGaO_2$ powders in deionized water. B) The ion-exchange reaction of $KGaO_2$ and CH_3COOH occurs at room temperature, the GaOOH nanosheets with dominant {100} facets form and grow. C) The GaOOH nanosheets assemble along the {011} facet. D) Formation of the GaOOH nanoplate with a rhombic cross section. E) Hydrothermal ion-exchange of the GaOOH nanoplate and Zn^{2+} takes place at a very slow speed and the $ZnGa_2O_4$ phase forms, based on the GaOOH nanoplate. F) Formation of the $ZnGa_2O_4$ nanocube.

Indeed, we can see that, in the final reaction product from reaction of GaOOH nanoplate and Zn^{2+}, the $ZnGa_2O_4$ nanoparticles are visible and pores (Figure 2b) existed on the surface of the $ZnGa_2O_4$ nanocubes, which resulted from the fact that the fast phase transformation caused the $ZnGa_2O_4$ nanoparticles to break off from the $ZnGa_2O_4$ nanocube. In addition, as is mentioned above, using the semifinished GaOOH single crystal nanoplate product as the precursor or directly heating the mixed solution of $KGaO_2$, CH_3COOH, and $Zn(CH_3COO)_2$, the final product formed was $ZnGa_2O_4$ nanocrystals with no specific morphology due to the fast reaction. The semifinished product of GaOOH presented more microstructures due to the expose of growing crystal facets (see Figure S7a in the Supporting Information), thus having a much higher reaction rate than the complete GaOOH nanoplate with the Zn^{2+}. The fast formation of $ZnGa_2O_4$ nanocrystals is more obvious in the mixed solution of $KGaO_2$, CH_3COOH, and $Zn(CH_3COO)_2$ due to the fast ion-exchange for the water soluble precursors. This also suggests that the GaOOH nanoplate reacting with Zn^{2+} has a moderate reaction rate for the formation and growth of $ZnGa_2O_4$ nanocubes. To confirm this, a GaOOH microrods of 5 μm in length and 500 nm cross section were prepared according to a previously reported method,[9] and were used as the precursor to synthesize $ZnGa_2O_4$ nanocubes. The GaOOH microrods reacted with Zn^{2+} about two times slower than the GaOOH nanoplates (see Figure S9 in the Supporting Information), indicating that the GaOOH precursor can control the formation rate of $ZnGa_2O_4$, and thus plays an important role in the final $ZnGa_2O_4$ morphology.

On the basis of these observations, the formation mechanism of the GaOOH nanoplates and $ZnGa_2O_4$ nanocubes can be illustrated as shown in **Figure 3**. The $KGaO_2$ solid powder was dispersed into water to form a colloidal suspension. Introducing the H^+ into $KGaO_2$ colloidal suspension, the preferential growth of {100} facet was first formed and assembled along the {011} facet to form the GaOOH nanoplate. This reaction of the the GaOOH nanoplate precursor and Zn^{2+} occurs on the GaOOH nanoplate under hydrothermal conditions to form the $ZnGa_2O_4$ nanocube.

2.3. Photocatalytic Performance of $ZnGa_2O_4$ Nanocube in the Water Splitting and CO_2 Reduction

Here, the $ZnGa_2O_4$ nanocube was used as a photocatalyst to split water as well as to convert CO_2 into CH_4. The $ZnGa_2O_4$ nanocube was heated at 550 °C for 4 h to clean the surface before performing the photoinduced reaction. For comparison, the mesoporous $ZnGa_2O_4$ was synthesized by the hydrothermal ion-exchange reaction of $ZnSO_4$ and $NaGaO_2$ at 200 °C for 5 h, a similar hydrothermal process as described in our previous report.[10] From **Figure 4**a, the $ZnGa_2O_4$ nanocube (CH_4: 0.16 μmol h^{-1}) shows a higher activity than mesoporous $ZnGa_2O_4$ (CH_4: 0.018 μmol h^{-1}). Brunauer–Emmett–Teller (BET) measurements revealed that the specific surface area of mesoporous $ZnGa_2O_4$ (S_{BET}: 92.4 m^2 g^{-1}) was about 10 times higher than that of the $ZnGa_2O_4$ cubes (S_{BET}: 9.5 m^2 g^{-1}). Therefore, the activity difference in CH_4 generation between the two samples cannot be attributed to the difference in specific surface area. TEM observation indicates that the mesostructure for the mesoporous $ZnGa_2O_4$ resulted from the agglomeration of about 10 nm nanocrystals with no specific morphology.[10]

A discussion of the carrier mobility of the two single-crystal samples, $ZnGa_2O_4$ nanocubes and $ZnGa_2O_4$ nanocrystals, is important. We constructed two theoretical models, {100} facet exposed $ZnGa_2O_4$ and bulk-$ZnGa_2O_4$, to understand the activity difference in CH_4 generation. Our calculations indicated that the electron effective mass for the two samples was very close to be 0.32 m_o (m_o is the mass of free electron). However, the hole effective mass of the $ZnGa_2O_4$ {100} facet (1.55 m_o) is about 2 times lighter than that of bulk-$ZnGa_2O_4$ (3.16 m_o). The

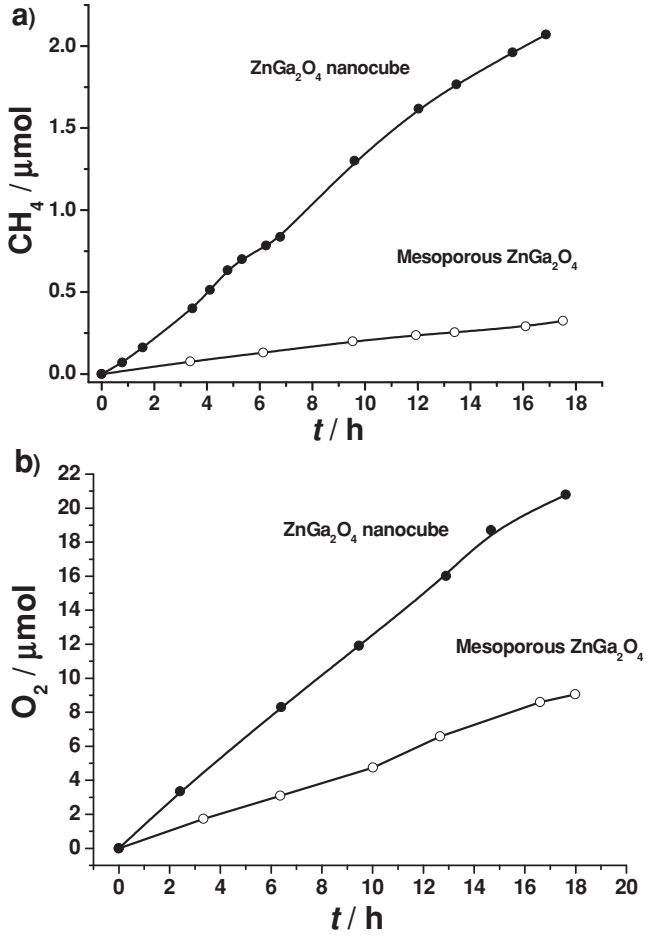

Figure 4. Generation of the gaseous products over various $ZnGa_2O_4$ during the CO_2 photoreduction under UV-vis light irradiation: a) CH_4 and b) O_2. (The units shown in y-axis in Fig.4a and b are wrong format, should be corrected as "μmol")

hole effective mass is obtained by calculating the coefficient of the k^2 term of $E(k) = h^2k^2/2\ m_h$ (where, E is the band energy, k is the wavevector, h is the Planck constant, and m_h is the hole effective mass). From this equation, it is clear that the exposed crystal surfaces with different atom distributions will induce different energy band structures, and thus have a different hole effective mass. For comparison, the hole effective mass for two typical facets of $ZnGa_2O_4$, {110} and {111}, was also calculated. The calculated hole effective mass was 1.71 m_o for {110} and 1.84 m_o for {111} facets, which were significantly lighter than 3.16 m_o for bulk $ZnGa_2O_4$, and slightly heavier than the 1.55 m_o for {100} facets. In the cubic $ZnGa_2O_4$ crystal, the {100}, {110}, and {111} facets exhibit the GaO, GaO_2, and Ga terminations, respectively, which cause the change in the hole effective mass.

A light-hole effective mass usually induces a high hole mobility. For CO_2 photoreduction with H_2O as the reducing agent, water was oxidized by photogenerated holes into O_2 and this process provided the protons and electrons to induce the reduction of CO_2 into hydrocarbons. Apparently, the high hole mobility is beneficial for promoting water oxidation. Indeed, the O_2 generation rate over the $ZnGa_2O_4$ nanocubes is about 3 times higher than that over the $ZnGa_2O_4$ (Figure 4b), thus the $ZnGa_2O_4$ nanocube with exposed {100} facets exhibited a higher CH_4 generation rate than the mesoporous $ZnGa_2O_4$. Usually, loading a co-catalyst on the surface of a photocatalyst can improve the photocatalytic activity. The CO_2 photoreduction over 0.5 wt% RuO_2-loaded $ZnGa_2O_4$ nanocubes was performed, and the conversion rate from CO_2 to CH_4 was determined to be 2.6 μmol h^{-1}, about 2 times higher than the unloaded nanocubes due to the improved separation of photogenerated electron-hole pairs.

In addition, for the CO_2 photoreduction into CH_4, in the gaseous products, the mole ratio of O_2 to CH_4 should be 2:1 according to the total reaction equation $CO_2 + 2H_2O \rightarrow CH_4 + 2O_2$. However, during the reaction, generated rate of detected O_2 was about 1.2 μmol h^{-1} which is about 7.5 times higher than that of CH_4 (0.16 μmol h^{-1}). The stoichiometric imbalance for O_2 to CH_4 suggests that other reduction products besides CH_4 form. Indeed, the low content of CO can be detected in the gaseous products.

Interestingly, using the $ZnGa_2O_4$ nanocube to split pure water, the detected gaseous product is hydrogen only. The hydrogen generation rate over the $ZnGa_2O_4$ nanocube is about 120 μmol h^{-1}, is about 3 times higher than mesoporous $ZnGa_2O_4$ (30 μmol h^{-1}) (**Figure 5**a). Usually, under light irradiation, the photogenerated electrons and holes thus produced diffuse to the surface and react with surface species. In our case, the photogenerated electrons were trapped by adsorbed water molecular to generate the hydrogen. However, no oxygen was detected during the light irradiation. A possible product from surface adsorbed water reacting with photogenerated holes is the hydroxyl free radical (•OH).[11] Recently, using the low temperature scanning tunneling microscopy (STM) performed at 80 K, Hou et al. observed the dissociation of individually adsorbed water molecules at the TiO_2 {110} surface.[12] Their results suggested that the initial step of the water dissociation under the UV light irradiation may not be reduced by the electrons, but most likely oxidized by the holes generated

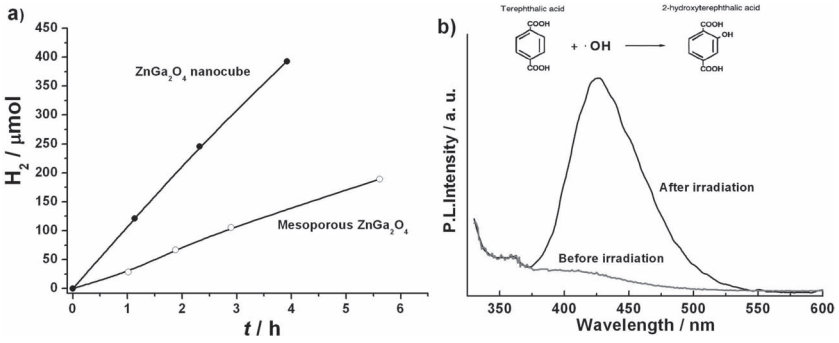

Figure 5. a) H_2 generation over various $ZnGa_2O_4$ under UV-vis light irradiation. b) Fluorescence spectral changes observed during UV illumination of $ZnGa_2O_4$ nanocube in terephthalic acid solution (4×10^{-4} M, excitation at 315 nm). Inset shows the formation of 2-hydroxyterephthalic acid as a result of the reaction between terephthalic acid and •OH.

by the photons to form the •OH radicals. This indicated that oxidizing water into •OH by photogenerated holes is an important reaction step for the water splitting. The valence band level of $ZnGa_2O_4$ was at 3.13 V vs NHE,[6] which is more positive than E^o(•OH/H_2O) (2.7 V vs NHE). This indicates that the holes photogenerated on irradiation of $ZnGa_2O_4$ can react with adsorbed H_2O to produce •OH. To determine the product from the water oxidation by photogenerated holes, we used terephthalic acid as a fluorescence probe to detect the •OH. Adding terephthalic acid (0.166 g) and NaOH (0.16 g) into the 200 mL of deionized water containing 0.1 g of $ZnGa_2O_4$ nanocube powder, after 30 min UV light irradiation, the fluorescence peak at 425 nm can be detected due to formation of 2-hydroxyterephthalic acid as a result of the reaction between terephthalic acid and •OH (Figure 5b), confirming that the •OH formed during the light irradiation.

As is well known, water splitting into hydrogen and oxygen gases involves a four-electron process. In our case, the water was oxidized into •OH ($h^+ + H_2O \rightarrow$ •OH + H^+) by holes and reduced into H_2 ($2e^- + 2H^+ \rightarrow H_2$) by electrons. This reaction is a two-electron process, thus having more favorable reaction kinetics compared to the four-electron water splitting process. It should be pointed out that the CO_2 photoreduction into CH_4 involving an eight-electron process is more complex than water splitting. Therefore, the hydrogen production (120 μmol h^{-1}) from water splitting is about 750 times higher than CH_4 generation (0.16 μmol h^{-1}) from CO_2 reduction due to the limitation in reaction kinetics. It is interesting to understand why water was oxidized to O_2 for CO_2 photoreduction and •OH for water splitting, respectively. It was found that bicarbonate and carbonate ions are effective hydroxyl free radical scavengers.[13] For CO_2 photoreduction using water as the reducing agent, the bicarbonate and carbonate radicals can be formed when the CO_2 molecules diffuse to meet the H_2O molecules, which can effectively suppress the formation of •OH.

3. Conclusions

A new route for preparing $ZnGa_2O_4$ nanocubes with exposed {100} facets has been demonstrated. The reaction pathway involves an ion-exchange process by using GaOOH single crystal nanoplates as the precursor. The $ZnGa_2O_4$ nanocubes exhibited high activities for CO_2 photoreduction to CH_4 as well as for water splitting into H_2 and •OH. Theoretical analysis indicated that the $ZnGa_2O_4$ nanocube has a light hole effective mass on the exposed {100} facets, which promotes water oxidation, thus improving the CH_4 generation rate for the photoreduction of CO_2.

4. Experimental Details

Synthesis and Characterization: The $KGaO_2$ solid powders were prepared by heating a stoichiometric mixture of K_2CO_3 and Ga_2O_3 at 850 °C for 12 h. GaOOH nanoplates were synthesized by an ion-exchange reaction of $KGaO_2$ and CH_3COOH. The $KGaO_2$ powder (0.002 mol) was dispersed in deionized water (30 mL) to obtain a colloidal solution. Then, 40 mL of CH_3COOH (0.002 mol) aqueous solution was added into the $KGaO_2$ colloidal solution. The resulting mixture was magnetically stirred at room temperature (35 °C) for 8 h. The final product was separated by centrifugation and dried at 60 °C for 2 h. For the preparation of $ZnGa_2O_4$ nanocube, in a typical procedure, the 0.002 mol of GaOOH nanoplate was added into 30 mL of $Zn(CH_3COO)_2$ (0.001 mol) aqueous solution and stirred for 10 min at room temperature, then the mixture was heated in a Teflon-lined hydrothermal autoclave at 200 °C for 20 h. The final product was separated by centrifugation and dried at 60 °C for 2 h. The crystallographic phase of these as-prepared products was determined by powder XRD (Rigaku Ultima III, CuKa radiation). The products were further investigated by surface area and porosity analyzer (Micromeritics TriStar, USA) and high-resolution transmission electron microscopy (FEI Tecnai G2 F30 S-Twin, USA).

Photocatalytic Tests: In the photocatalytic reduction of CO_2, 0.1 g of $ZnGa_2O_4$ nanocubes was uniformly dispersed on the glass reactor with an area of 4.2 cm^2. An UV-enhanced (200 to 350 nm) 300 W Xenon arc lamp was used as the light source of photocatalytic reaction. The volume of reaction system was about 230 mL. After the reaction setup was vacuum-treated several times, the high purity of CO_2 gas was followed into the reaction setup, and then, 1 mL of deionized water was injected as a reducing reagent, which can evaporate to form the gaseous water under the heating of the light. The reaction setup was kept at ambient pressure. During irradiation, about 0.5 mL of gas was continually taken from the reaction cell at given time intervals for subsequent CH_4 concentration analysis by using a gas chromatograph (GC-14B; Shimadzu Corp., Japan). For the water splitting, 0.3 g of $ZnGa_2O_4$ nanocubes was dispersed in 390 mL of deionized water by a magnetic stirrer in an inner irradiation cell made of quartz. The light source was a 400 W high-pressure mercury lamp (SEN; HL400EH-5). The gas amounts of H_2 from H_2O splitting were determined using gas chromatography (Shimadzu; GC-8A, MS-5A column, TCD, Ar carrier). To detect the formation of •OH, fluorescence spectroscopy performed (Cary eclipse fluorescence spectrophotometer (USA)).

Theoretical Calculations: To understand the photophysical properties of bulk-$ZnGa_2O_4$ and {100} facets exposed $ZnGa_2O_4$ nanocube, first principles calculations were performed using the VASP[14] code with projected augmented wave (PAW) method.[15] Generalized gradient approximation (GGA)[16] in the scheme of Perdew–Bueke–Ernzerhof (PBE)[17] was used for the exchange correlation function. The valence electronic configurations of $2s^22p^4$ for O, $3d^{10}4s^2$ for Zn and $3d^{10}4s^24p^1$ for Ga were used to generate the pseudopotentials. Geometry relaxation was performed until the residual forces acting on each ion were less than 0.02 eV $Å^{-1}$. The bulk-$ZnGa_2O_4$ model was constructed using a supercell including the Zn8, Ga16, and O32. The {100} surface of $ZnGa_2O_4$ has two different terminations ({100}-Zn and {100}-GaO). According to the calculated surface energy, the {100}-GaO termination was chosen to describe the {100} surface model of $ZnGa_2O_4$ due to the low surface energy. All atoms were allowed to relax during geometry relaxation. A 500 eV of cutoff energy and a Monkhorst–Pack k-point mesh of 4 × 4 × 1 were used for surface model. After testing, the surface model was constructed using 9 alternating layers, which was sufficient for simulating surface properties. To compare the carrier mobility between {100}-GaO surface and the bulk model, we calculated the minimum effective electron mass in the conduction band (m_e) and maximum effective mass of hole in valence band (m_h) . For {100}-GaO surface and bulk model, K points path in Brillouin zone for band structures calculation was Γ(0.0, 0.0, 0.0)-F(0.0, 0.5, 0.0)-Q(0.0, 0.5, 0.5)-Z(0.0, 0.0, 0.5)-Γ(0.0, 0.0, 0.0). For the {100}-GaO surface, m_e and m_h were calculated along Γ-F. For the bulk model, m_e and m_h were calculated along Γ-F and F-Q, respectively.

Supporting Information

Supporting Information is available from the Wiley Online Library or from the author.

Acknowledgements

This work is supported by the National Basic Research Program of China (2013CB632404), the National Natural Science Foundation of

China (Nos. 51102132, 11174129, and 21073090), the Priority Academic Program Development of Jiangsu Higher Education Institutions, and the Jiangsu Provincial Funds for Distinguished Young Scientists (No. BK2012015).

Received: July 23, 2012
Revised: August 20, 2012
Published online: September 14, 2012

[1] H. Tong, S. X. Ouyang, Y. P. Bi, N. Umezawa, M. Oshikiri, J. H. Ye, *Adv. Mater.* **2012**, *24*, 229.
[2] H. G. Yang, C. H. Sun, S. Z. Qiao, J. Zou, G. Liu, S. C. Smith, H. M. Cheng, G. Q. Lu, *Nature* **2008**, *453*, 638.
[3] C. C. Yang, Y. H. Yu, B. van der Linden, J. C. S. Wu, G. Mul, *J. Am. Chem. Soc.* **2010**, *132*, 8398.
[4] a) K. Ikarashi, J. Sato, H. Kobayashi, N. Saito, H. Nishiyama, Y. Inoue, *J. Phys. Chem. B* **2002**, *106*, 9048; b) X. Chen, H. Xue, Z. H. Li, L. Wu, X. X. Wang, X. Z. Fu, *J. Phys. Chem. C* **2008**, *112*, 20393.
[5] a) K. W. Chang, J. J. Wu, *J. Phys. Chem. B* **2005**, *109*, 13572; b) P. Feng, J. Y. Zhang, Q. Wan, T. H. Wang, *J. Appl. Phys.* **2007**, *102*, 074309; c) Y. J. Li, M. Y. Lu, C. W. Wang, K. M. Li, L. J. Chen, *Appl. Phys. Lett.* **2006**, *88*, 143102.
[6] S. C. Yan, S X. Ouyang, J. Gao, M. Yang, J. Y. Feng, X. X. Fan, L. J. Wan, Z. S. Li, J. H. Ye, Y. Zhou, Z. G. Zou, *Angew. Chem. Int. Ed.* **2010**, *49*, 6400.
[7] A. W. Laubengayer, H. R. Engle, *J. Am. Chem. Soc.* **1939**, *61*, 1210.
[8] a) J. Tian, L. V. Saraf, B. Schwenzer, S. M. Taylor, E. K. Brechin, J. Liu, S. J. Dalgarno, P. K. Thallapally, *J. Am. Chem. Soc.* **2012**, *134*, 9581; b) Q. X. Yao, J. L. Sun, K. Li, J. Su, V. Peskov, X. D. Zou, *Dalton Trans.* **2012**, *41*, 3953.
[9] J. Zhang, Z. G. Liu, C. K. Lin, J. Lin, *J. Cryst. Growth* **2005**, *280*, 99.
[10] S. C. Yan, Z. Q. Wang, Z. S. Li, Z. G. Zou, *J. Mater. Chem.* **2011**, *21*, 5682.
[11] a) R. I. Bickley, F.S. Stone, *J. Catal.* **1973**, *31*, 389; b) R. I. Bickley, V. Vishwanathan, *Nature* **1979**, *280*, 306; c) H. V. Damme, W. K. Hall, *J. Am. Chem. Soc.* **1979**, *101*, 4373; d) P. F. Schwarz, N. J. Turro, S. H. Bossmann, A. M. Braun, A.-M. A. Abdel Wahab, H. Dürr, *J. Phys. Chem. B* **1997**, *101*, 7127; e) C. S. Turchi, D. F. Ollis, *J. Catal.* **1990**, *122*, 178.
[12] S. J. Tan, H. Feng, Y. F. Ji, Y. Wang, J. Zhao, A. D. Zhao, B. Wang, Y. Luo, J. L. Yang, J. G. Hou, *J. Am. Chem. Soc.* **2012**, *134*, 9978.
[13] D. R. Mccracken, G. V. Buxton, *Nature* **1981**, *292*, 439.
[14] a) G. Kresse, J. Furthmuller, *Comput. Mater. Sci.* **1996**, *6*, 15; b) G. Kresse, J. hafner, *Phys. Rev. B* **1993**, *47*, 558.
[15] P. E. Blochl, *Phys. Rev. B* **1994**, *50*, 17953.
[16] J. P. Perdew, J. A. Chevary, S. H. Vosko, K. A. Jackson, M. R. Pederson, D. J. Singh, C. Fiolhais, *Phys. Rev. B* **1992**, *46*, 6671.
[17] J. P. Perdew, K. Bruke, M. Ernzerhof, *Phys. Rev. Lett.* **1996**, *77*, 3865.